

Reduced graphene oxide-poly(methyl methacrylate) nanocomposite as a supercapacitor

Zabiholah Zabihi,¹ Paul Eduardo David Soto Rodriguez,² Abderrahmane Boujakhrou,² Juan Carlos Viera,³ Jorge Alonso del Valle,³ Houshang Araghi,¹ Reynaldo Villalonga²

¹Department of Physics, Amirkabir University of Technology, Tehran, Iran

²Department of Analytical Chemistry, Universidad Complutense de Madrid, Ciudad Universitaria s/n 28040, Madrid, Spain

³Department of Electrical and Electronic Engineering, University of Oviedo, Campus de Viesques, s/n, Edificio Departamental 3 33204, Gijón Asturias, Spain

Correspondence to: H. Araghi (E-mail: araghi@aut.ac.ir)

INTRODUCTION

Compared to traditional batteries used for energy storage applications, the so-called supercapacitors and ultracapacitors present superior properties in terms of power density, charge-discharge rates, and stability (long life-cycle performances)¹⁻³ and have attracted attention in this field, especially for electrochemical energy storage devices. They are potential candidates to complement or eventually replace common batteries used in energy storage applications, such as for portable and wearable electronic devices and for electric and hybrid vehicles.⁴ The supercapacitors are classified according to their energy storage mechanism into two main categories: (1) electric double-layer capacitors (EDLCs) and (2) pseudocapacitors.⁵ In EDLCs, the capacitance originates from the accumulation of charges at the electrode-electrolyte interfaces. Therefore, controlling the specific surface area and pore size and enhancing electrical conductivity are the effective ways to achieve a high storage capacity.⁶ The second category is related to the energy storage of pseudocapacitance, where the storage mechanism occurs by transferring the faradic charges between electrolyte and electrode by

reversible multielectron redox faradic reactions, producing higher specific capacitance and energy density than EDLCs.⁷⁻⁹ However, the poor electrical conductivity observed in pseudocapacitive electrodes can restrict the faradic reactions, therefore leading to unsatisfactory electrochemical performance and life cycles. To overcome this, several combinations of materials have been investigated to take advantage of their individual intrinsic properties; among these, the combination of metal oxide and graphene to improve electrochemical performance has been widely investigated.^{10,11} Instead, here the fabrication of an electrode based on a nonconductive polymer such as poly(methyl methacrylate) (PMMA; providing a large surface area) is investigated by studying how the electrical conductivity conferred by the conductive nanocomposites (graphene and metal hybrid) and their inclusion act on the electrode electrochemical performance.

Three types of materials can be distinguished that are used in the fabrication of supercapacitor electrodes: carbon-based materials,¹²⁻¹⁷ transition metal oxides,¹⁸⁻²⁷ and conductive polymers.²⁸⁻³⁰ Carbon-based materials are most frequently used for

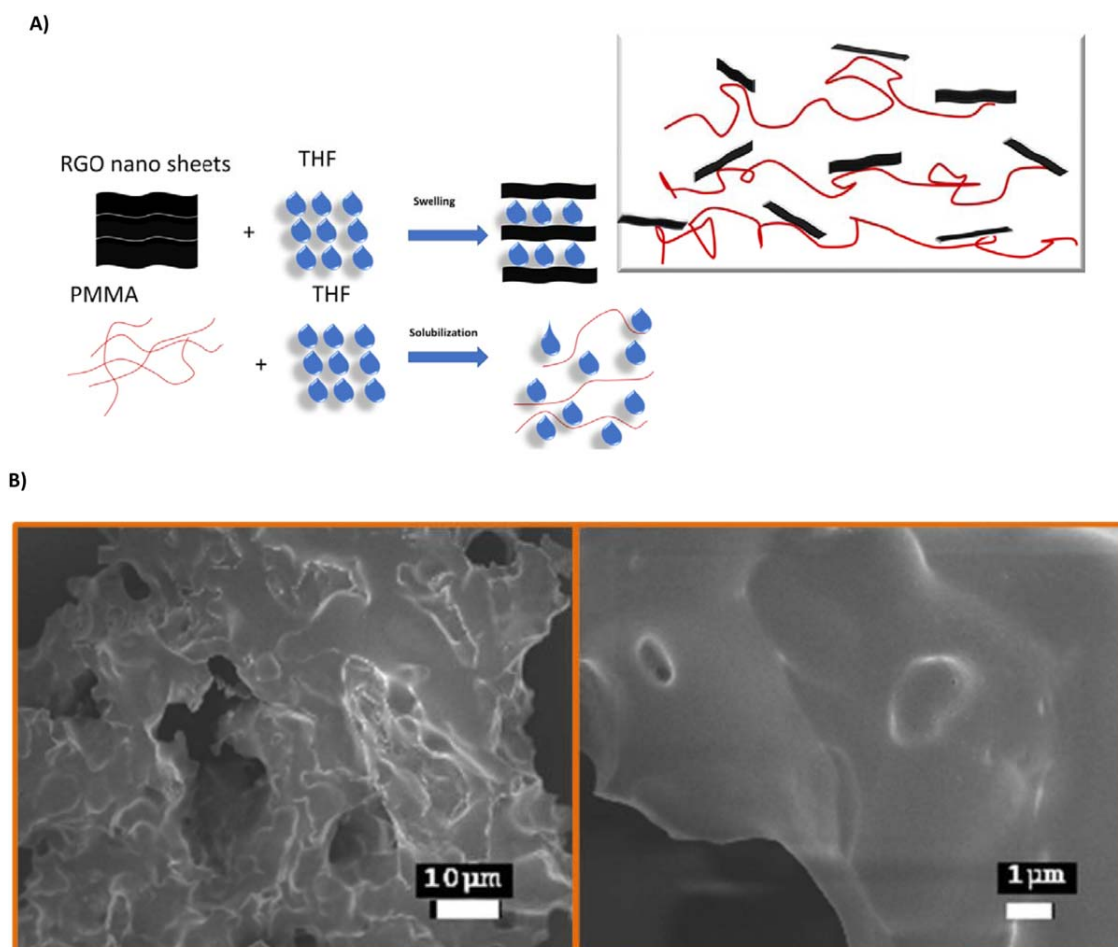


Figure 1. (A) Illustration of the RGO/PMMA synthesis process; (B) SEM image of 2% RGO/PMMA. [Color figure can be viewed at wileyonlinelibrary.com]

electric double-layer capacitors, wherein the charge storage process is nonfaradic and the storage of energy is electrostatic. In particular, graphene-based materials are promising for energy storage applications because of their unique intrinsic properties: a highly tunable surface area, excellent electrical conductivity, high chemical stability, and superior mechanical behavior. Conductive polymers such as polyaniline (PANI), on the other hand, are shown to have more pseudocapacitor behavior like metal oxides.⁶

The rise of universal, wearable, portable, and flexible electronics comes with innovative demands for novel energy storage solutions. Due to the inherently flexible polymeric nature of conductive polymers, they have drawn a great deal of interest for flexible supercapacitor applications.³¹ Many material combinations, and on different length scales (0D, 1D, 2D, and 3D structures), have been the subject of study. The focus of this work is on graphene nanocomposites immersed in a nonconductive polymer matrix such as PMMA. Here, the nanocomposites used are reduced graphene oxide (RGO) and (3-Aminopropyl) triethoxysilane (APTES)-functionalized reduced graphene oxide (G) composites. As these nanocomposites are capable of conferring electrical conductivity to the matrix, we explore the effect of different percentage additions of nanocomposite and analyze

their electrochemical behavior in different aqueous electrolytes: KCl, NaCl, NaOH, and H₂SO₄. A faradic current is observed under slow scan rates for RGO with NaOH and KCl electrolytes, indicating significant electron charge transfer occurs in these electrolytes. In addition, for functionalized RGO in KCl, an electrochemical double-layer capacitance is observed. This facile change from faradic to EDLC behavior upon nanocomposite functionalization, together with their low cost and beneficial mechanical properties (from the intrinsic flexible polymer nature), is extremely appealing for hybrid supercapacitor ensembles. Therefore, proposed electrodes are explored for their use as supercapacitors, and as such, an optimum nanocomposite filling percentage is found for which the highest faradic peak is measured and in which the highest energy is stored. The capacitance values obtained are compared to similar materials showing a good overall energy storage performance. For this comparison, similar systems were taken into consideration, that is, conductive materials in a nonconductive matrix.

All materials were prepared by wet chemical methods and characterized by means of scanning electron microscopy (SEM), differential scanning calorimetry (DSC), Fourier transform infrared (FTIR), cyclic voltammetry (CV), and electrochemical impedance spectroscopy (EIS).

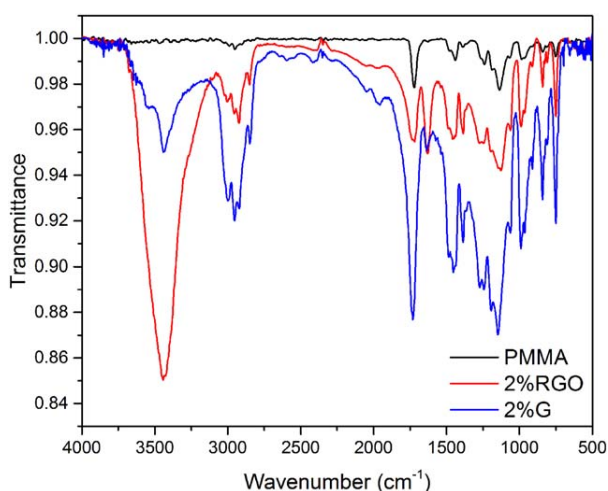


Figure 2. FTIR spectra of PMMA and 2 wt % RGO/PMMA and 2 wt % RGO/PMMA composites. [Color figure can be viewed at wileyonlinelibrary.com]

EXPERIMENTAL

Preparation of Reduced Graphene Oxide

The synthesis of the RGO suspension was realized according to the work presented by Park *et al.*³² For this, graphene oxide (60 mg) was mixed with 20 mL of distilled water and sonicated in an ultrasound bath (250 W) for 2 h to obtain a homogenous GO suspension. For the final reduction, 180 mL of *N,N*-dimethylformamide (DMF) and 5 μ L of hydrazine monohydrate per 12 mg of GO were added to the GO suspension and heated to 80 °C for a period of 2 h, yielding a black suspension that was thereafter sonicated for 5 min. Several RGO suspensions with different reduction states were prepared. This was done by changing the volume of the reductant (hydrazine monohydrate). The RGO suspension was filtered and washed with ethanol (three times) to obtain a solid RGO.

Preparation of RGO/PMMA Nanocomposites

The RGO/PMMA nanocomposites were prepared by a solution intercalation method [a schematic is presented in Figure 1(A)]. A PMMA solution was prepared by dissolving PMMA powder in tetrahydrofuran (THF). The solid RGO solution was dissolved in THF at appropriate concentrations. Separately, both the RGO solution and PMMA solution were sonicated for 1 h. Afterward, the RGO solution was added into the PMMA solution, and the mixture was stirred for 1 h. A well-dispersed RGO/PMMA composite solution was then obtained. The final solution was poured under vigorous stirring into a beaker or jar filled with methanol. The precipitate was filtered and then washed with ethanol three times. The solid was dried in a vacuum for 12 h.³³

Electrode Preparation and Measurements

For the nanocomposite electrode, a 1 mg/mL solution of nanocomposite in ethanol was prepared, and of this 10 μ L was drop-cast on the carbon working electrode (0.1256 cm²) of a three-electrode screen-printed electrode (SPE; Orion High Technologies, Parla, Madrid, Spain, product OHT-000) and left to dry. All electrochemical (except the galvanostatic charge–discharge)

measurements were done with a potentiostat (Autolab PGSTAT 302N, Metrohm Autolab, Utrecht, The Netherlands.).

Galvanostatic Charge–Discharge Characterization

To study the galvanostatic charge–discharge cycles, a Keithley SourceMeter (model 2440, Cleveland, OH) was connected to the SPE, applying a fixed current of 5 μ A, and simultaneously the potential was read out. LabVIEW (Laboratory Virtual Instrument Engineering Workbench), a software from National Instruments (Austin, TX) was set up to program the cycles. The potential limits were taken from the CV measurements in which the value for the reference potential was taken into account.

RESULTS AND DISCUSSION

Morphological and Structural Characterization

For the SEM images, a JEOL 7600 SEM (Tokyo, Japan) was used. The images were taken at 5 kV and magnifications of 500 \times and 4000 \times . The SEM images of 2% RGO/PMMA under both magnifications are shown in Figure 1(B). The film presents a large surface area, as expected for PMMA. Due to its low conductivity, a thin layer of gold was sputtered on top to enhance the contrast image.

Figure 2 shows the FTIR spectra of PMMA and the 2 wt % RGO/PMMA and 2 wt % G/PMMA composites. FT-IR spectra were acquired with a Nicolet Nexus 670/870 spectrometer (Thermo Fisher

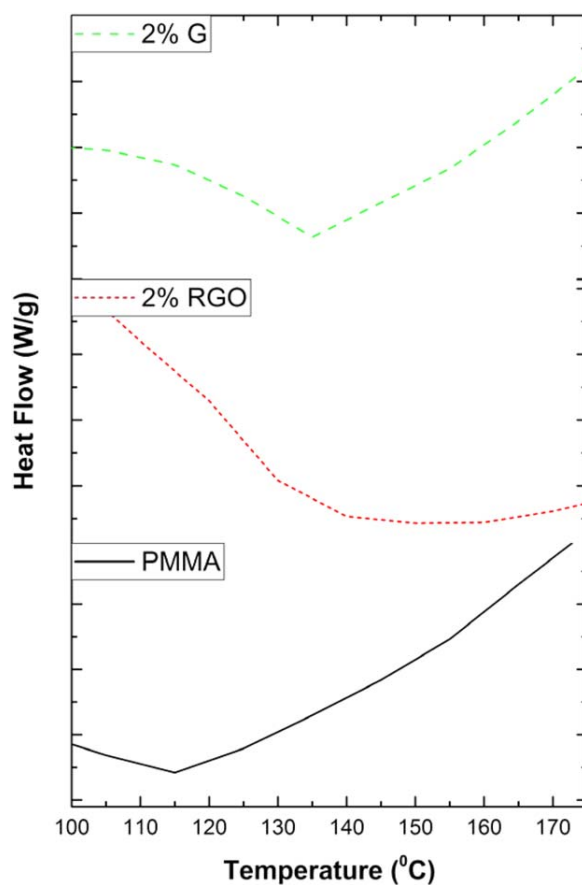


Figure 3. DSC thermograms of bare PMMA and PMMA with 2 wt % G or 2 wt % RGO recorded after second heating, at a heating rate of 10 °C/min in nitrogen atmosphere. [Color figure can be viewed at wileyonlinelibrary.com]

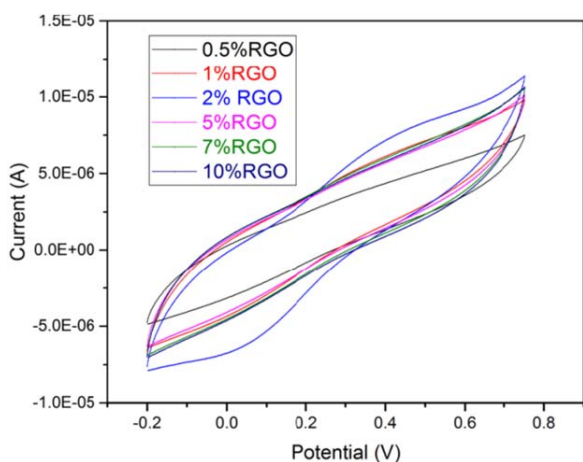


Figure 4. Different percentages of RGO nanocomposites in 1 M KCl. [Color figure can be viewed at [wileyonlinelibrary.com](#)]

Scientific, Waltham, Massachusetts USA). For the bare PMMA, the spectrum showed characteristic bands at 2998, 1728, and 1143 cm^{-1} , which correspond to the aliphatic C—H, C=O, and C—O—C groups, respectively. In contrast, the FTIR spectra from Figure 2 show that the inclusion of nanocomposite (2 wt % RGO and G) leads to representative peaks at 3442, 1719, and 1629 cm^{-1} , which correspond to the O—H, C=O, and C=C groups, respectively. (The peak at 2922 cm^{-1} corresponds to the C—H groups. The bands between 1270 cm^{-1} and 990 cm^{-1} originate from the C—O group.) This proves the presence of RGO and G in the PMMA.

In Figure 3 the DSC curves for bare PMMA and PMMA with 2 wt % G and 2 wt % RGO are presented. The glass-transition temperatures for PMMA and PMMA with 2 wt % G and 2 wt % RGO were determined to be 115, 135, and 140 $^{\circ}\text{C}$, respectively. These values are in agreement with that obtained in a previous experimental study.³⁴

Electrochemical Characterization

Cyclic Voltammetry. To observe which electrochemical behavior dominates (i.e., which current dominates: faradic or capacitive), the electrodes were analyzed by cyclic voltammetry. The CV curve is shown in Figure 4 for a fixed scan rate of 150 mV/s and in a 1 M KCl electrolyte for the case of RGO at different concentrations. It shows a clear optimum value (2%) at which both the redox-related cathodic and anodic peak currents are maximized. Even more, at higher concentrations it is constant. Therefore we consider the 2% nanocomposite filling as optimum; it presents a well-defined redox reaction (faradic peaks), suggesting a pseudocapacitance behavior.

Faradic peaks are an indication that electron transfers are occurring at the interface, though it generally depends on the electrolyte used. For this reason, different electrolytes were studied for the 2% RGO nanocomposite, and the results are shown in Figure 5. In comparison to 1 M KCl electrolyte, the RGO nanocomposite/PMMA electrode (CV curves with different scan rates are presented in Figure S1 in the Supporting Information) did not show a faradic reaction in the 0.1 M KCl nor in the 0.1 M H_2SO_4 ; although a small reduction peak appears, it disappears at higher scan rates

(Figure S2). However, for NaOH, clear oxidation and reduction current peaks are observed, indicating that faradic currents are present. In addition, the results for 2% G are shown. In contrast to the RGO in the 0.1 M KCl electrolyte, the CV curve is more square, as would be expected for an EDLC, and also the overall current increases compared to the RGO case, which leads to a higher capacitance (2.23 F/g). For 0.1 M H_2SO_4 , the CV curve shows neither an evident faradic current peak nor a square-like shape, and in 0.1 M NaOH only small prominent faradic peaks appear.

These observations indicate that G exhibits EDLC behavior in KCl electrolyte and RGO pseudocapacitance at 1 M KCl but not at 0.1 M, indicating that for this concentration the number of ions transferring charge to the electrode is too small to be measurable. Nevertheless, for the 0.1 M NaOH concentration, pseudocapacitance is clearly present, indicating that the related ion transfer is more effective. This fact might be related to a faster adherence of the ions to the electrode surface. In order to see if the cation Na^+ or the anion OH^- is responsible for the observed feature, the RGO/PMMA electrode was tested in 0.1 M NaCl electrolyte (see the Supporting Information), for which no faradic peaks were present, thus strongly suggesting that the OH^- anions are responsible for the observed pseudocapacitance.

As seen in the SEM images (Figure 1), the RGO/PMMA electrode film is not smooth, and therefore the accessibility of the ions toward the electroactive spots at the electrode surface (mainly by mass transport) will be dictated by the scan rate at which the CV measurements are performed, and hence the capacitance will change accordingly. The area of the CV curve represents the charge, being therefore proportional to the capacitance. Therefore, a variation in area of the CV curve is expected to be observed when the capacitance changes. Indeed, as can be seen from Figure 6, in which the CV curves at different scan rates for both 2% G and 2% RGO are shown, a more square-like shape (increasing area) for the case of G upon an increase in scan rate is seen, and an increase of the faradic current peaks (increasing area) for the case of RGO is observed.

The capacitance C is determined from the CV curves at different scan rates according to eq. (1)³⁵ and is presented in Table 1 together with capacitance values of similar systems (conductive elements in a nonconductive matrix) obtained in other works:

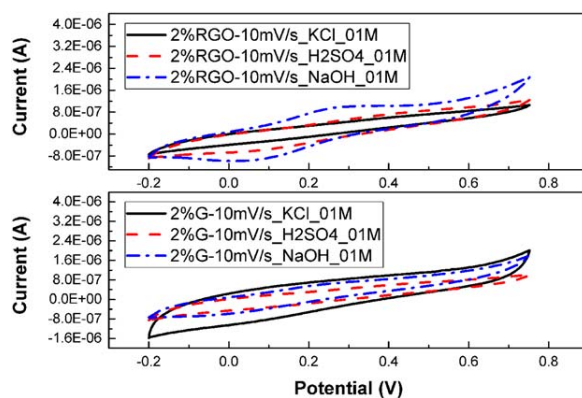


Figure 5. Different electrolytes KCl, H_2SO_4 , and NaOH for both 2% RGO (top) and 2% G (bottom) nanocomposites. [Color figure can be viewed at [wileyonlinelibrary.com](#)]

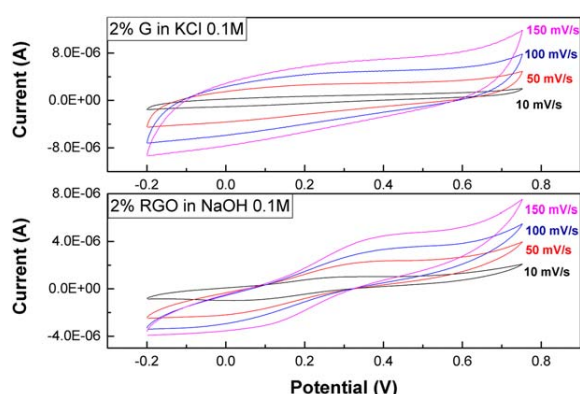


Figure 6. CV curves for 2% G in 0.1 M KCl (top) and 2% RGO in 0.1 M NaOH (bottom). [Color figure can be viewed at wileyonlinelibrary.com]

$$C = \frac{I_{ave}}{m \times s} \quad (1)$$

where I_{ave} is the current, s is the scan rate, and m is the mass of deposited material (~ 1 mg/mL).

Electrochemical Impedance Spectroscopy. In order to assess the ionic conductivity, a fast redox probe such as ferro/ferricyanide was used in a 1 M KCl electrolyte (for which the RGO showed pseudocapacitance and G an EDLC behavior). The corresponding Nyquist plot is shown in Figure 7. In the ideal case for a pure capacitor, the corresponding impedance response corresponds to a straight line being parallel to the imaginary axis of the Nyquist plot. However, in real capacitors, a high slope indicating a steeply rising capacitive impedance response is observed in the low-frequency region together with high-frequency semicircular features related to the bulk and interfacial properties. The increased

Table 1. Comparison of Specific Capacitance of PMMA Composite Electrodes to Other Electrodes

Material	Electrolyte	Specific capacitance (SC) (F/g)	Reference
Fe ₃ O ₄ electrode	1.0 M KOH	3	36
Perovskite SrRuO ₃	6 M KOH	8	37
RuO ₂	6 M KOH	20	37
La _{0.2} Sr _{0.8} RuO ₃	6 M KOH	21	38
Sb-doped SnO ₂ nanocrystallite thin film	1 M KOH	16	38
Indium oxide (In ₂ O ₃) nanospheres	1 M Na ₂ SO ₄	7.6	39
Carbon fibers (CF)	3 M KCl	0.06	40
Activated carbon fiber (ACF)	3 M KCl	2.63	40
Industrially activated carbon fiber (IACF)	3 M KCl	0.1	40
CF/PAN	PC/EC+0.1 M LiTFSI	0.003	40
ACF/PAN	PC/EC+0.1 M LiTFSI	0.055	40
IACF/PAN	PC/EC+0.1 M LiTFSI	0.026	40
CF/PEGDGE ^a	0.1 M LiTFSI	0.0045	40
ACF/PEGDGE	0.1 M LiTFSI	0.0014	40
CF/PEGDGE	0.1 M LiTFSI + IL	0.0111	40
ACF/PEGDGE	0.1 M LiTFSI + IL	0.0522	40
CFs by chemical activation with KOH	3 M KCl	3.27	41
CF ⁺ carbon nanotubes	3 M KCl	2.63	42
CF ⁺ carbon aerogels	3 M KCl	14	42
CNT fiber	Ionic liquid electrolyte	20–24	43
Graphene	0.5 N H ₂ SO ₄	14	44
As-received CF	3 M KCl	0.06 (0.01)	45
CAG ^b -modified (pressing) (CF + 22 wt % CAG)	3 M KCl	14.3 (0.2)	45
CAG-modified (infusion) (CF + 15.9 wt % CAG)	3 M KCl	8.7 (0.3)	45
CAG-modified (infusion scaled up) (CF + 9.5 wt % CAG)	3 M KCl	5.9 (0.4)	45
CNT+PANI	1 M H ₂ SO ₄	16	46
2%RGO/PMMA	1 M KCl	24.8	This work
2%RGO/PMMA	1 M NaOH	30.4	This work
2%G/PMMA	1 M KCl	15.08	This work
2%G/PMMA	1 M NaOH	25.6	This work

^a Poly(ethylene glycol) diglycidyl ether (PEGDGE)

^b Carbon aerogel (CAG)

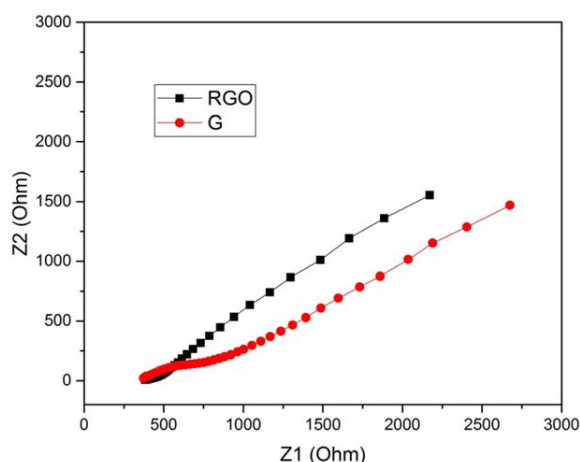


Figure 7. Nyquist plot for both 2% RGO (black curve) and 2% G (red curve). [Color figure can be viewed at wileyonlinelibrary.com]

semicircle observed in G indicates an increase in ionic resistance for G (red curve) over RGO. The steeper (higher slope) for RGO indicates a faster redox mechanism compared to that for G.

The corresponding plot of resistance versus nanocomposite weight percentage is shown in Figure 8. An inflection point close to 2% is observed for both nanocomposites, which also corresponds to the optimized weight percentage observed for the pseudocapacitance in 1 M KCl.

Electron Transport Model. A strong RGO-dependent behavior from the Nyquist plots is observed; see Figure 8. The addition of RGO in the composites results in a corresponding reduction in the size of the impedance planar plots, and it gradually decreases with increasing RGO concentration up to the incorporation of 2% RGO and then starts increasing. At low weight percentages, the average separation distance between RGO sheets is large. Thus, the electron transport paths are not formed within the PMMA matrixes. Therefore, the overall electrical conductivity of RGO/PMMA composites takes the values

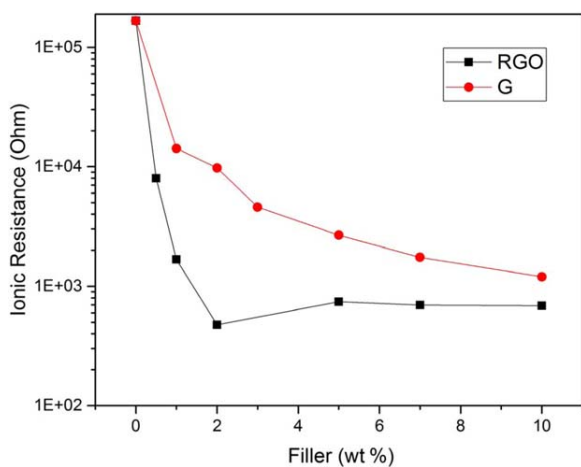


Figure 8. Ionic resistance, obtained from their corresponding Nyquist plots, for both RGO and G depending on the nanocomposite weight percentage. [Color figure can be viewed at wileyonlinelibrary.com]

of the PMMA matrix. When the weight percentage of nanofillers exceeds the critical weight percentage (percolation threshold), the electrical conductivity of RGO/PMMA composites increases by several orders of magnitude and, finally, will tend to be constant (percolation process). A quantum tunneling mechanism plays a dominant role in electrical transport in graphene-based composites. Simmons⁴⁸ derived a formula for the electrical tunneling effect between two electrodes separated by a thin insulating film (as electrodes we may consider on one side the electrolyte and at the other the carbon electrode sandwiching the PMMA nanocomposite thin film), and the tunneling-type contact resistances can be expressed as

$$I = \frac{2e}{h} \int_0^{\infty} T(E) M(E) [f(E - eV) - f(E)] dE \quad (2)$$

Here, Planck's constant is shown by h , e is electron charge, the symbol $M(E)$ denotes the total number of conduction channels, $T(E)$ is a transmission probability, and $f(E)$ is the Fermi–Dirac distribution function. Approximating asymptotically eq. (2) by means of the Sommerfeld expansion and considering a low bias voltage V , we find the resistance can be written as follows:

$$R = \frac{V}{I} = \frac{h}{2e^2} \times \frac{1}{M T} \quad (3)$$

By solving the Schrodinger equation for a polymer potential barrier with the Wentzel–Kramers–Brillouin (WKB) approximation,⁴⁷ it is possible to relate the transmission probability T of the electron, which gives the probability of an electron tunneling through the polymer potential barrier present between graphene layers, and the minimum distance between two neighboring graphene layers (d) and the height of the barrier (ϕ_{eff})^{48,49}:

$$T = \exp\left(-\frac{2\pi d}{h} \sqrt{8m_e \phi_{\text{eff}}}\right) \quad (4)$$

where

$$\phi_{\text{eff}} = \phi_0 - \left(\frac{V}{2d}\right)(s_1 + s_2) - \left[\frac{5.75}{K(s_1 - s_2)}\right] \ln\left[\frac{s_2(d - s_1)}{s_1(d - s_2)}\right] \quad (5)$$

$$s_1 = \frac{6}{K \phi_0} \quad (6)$$

$$s_2 = d \left[1 - \frac{46}{3\phi_0 K d + 20 - 2VKd}\right] \quad (7)$$

and m_e is the electron mass. By combining eqs. (3) and (4), we may determine the shortest distance between two graphene layers:

$$d = \frac{h}{2\pi\sqrt{8m_e \phi_{\text{eff}}}} \ln\left(\frac{2e^2}{h} MR\right) \quad (8)$$

The present model can describe the effect observed in Figure 8, where it is shown that as the nanofiller content increases, the resistance of the composite decreases. More specifically, this can be explained by eq. (8), which shows that as the minimum distance between graphene layers decreases, it becomes easier to construct a conductivity network [as the distance d is proportional to $\ln(MR)$].

Stability. In 1 M KCl, stable charge–discharge cycles at constant current (5 μA) were obtained and remained stable even over 900

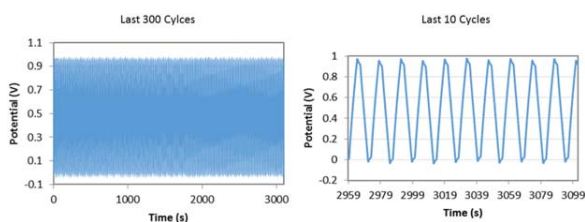


Figure 9. Last 300 and last 10 charge–discharge cycles at a constant current of 5 μA just after 900 cycles. [Color figure can be viewed at wileyonlinelibrary.com]

cycles. As an example, Figure 9 shows the last 300 and the last 10 cycles for the 2% RGO/PMMA supercapacitor. The tests were carried out using a Keithley 2440 SourceMeter. The resulting capacitances calculated from these cycles are in accordance with the values obtained by the CV measurements. The capacitance can be calculated by the following equation:

$$C = \frac{I_{\text{dis}} \times \Delta t_{\text{dis}}}{\Delta V_{\text{dis}}} \quad (9)$$

where I_{dis} corresponds to the discharge current, Δt_{dis} is the discharge time, and ΔV_{dis} is the maximum potential reached minus the ohmic drop.

CONCLUSIONS

An optimized filler weight percentage of 2% was observed for which pseudocapacitance was obtained for RGO in a 1 M KCl electrolyte and around which the inflection point of ionic resistance versus filler weight percentage was observed. Instead of pseudocapacitance, electrostatic electron transport (EDLC) is observed for functionalized RGO (G) in 0.1 M NaOH. The inclusion of RGO in the PMMA is equivalent, in an electrochemical manner, to a common conductive polymer such as PAN. A simple electron transport model is presented that explains the observed electronic measurements. In addition, we have determined that the RGO/PMMA conductive polymer has higher affinity toward OH^- ($r = 133 \text{ pm}$) anions than the other anions studied, both Cl^- ($r = 167 \text{ pm}$) and SO_4^- ($r = 258 \text{ pm}$), being thus related to an increased transport due to the smaller anion size. In this sense, the observed pseudocapacitance is no surprise as conductive polymers such as PANI show similar behavior. On the other hand, the observed EDLC for G must be directly related to the APTES functionalization, which changes the electrode surface functional groups, facilitating the electrochemical double-layer formation, and therefore the electrostatic charge transfer dominates over the observed redox reaction of the nonfunctionalized RGO nanocomposite. For the latter, stable (over 900 cycles) charge–discharge cycles have been observed, confirming their promising performance.

These results show that a low-cost nanocomposite PMMA supercapacitor can be easily fabricated, which opens the possibility to fabricate a hybrid supercapacitor combining electrodes based on RGO and functionalized G. In addition, these materials would be excellent candidates to be analyzed with a solid PMMA electrolyte to have an all-polymer supercapacitor, which in principle would allow a higher power as $P = IV^2$, so the potential window could be increased even further as compared to when an aqueous electrolyte is used (as here electrolysis is

the limitation). Also, it would permit fabrication of a highly flexible supercapacitor.

ACKNOWLEDGMENTS

Zabihollah Zabihi is grateful to the Department of Analytical Chemistry at Universidad Complutense de Madrid for hospitality during a nine-month visit, where the experimental part of this work was carried out. He is grateful to the Iran Ministry of Science, Research, and Technology for a fellowship in support of this visit. This work was supported in part by the Science and Innovation Spanish Ministry and FEDER under the projects DPI2013-046541-R, TIN2014-56967-R, and TEC2016-80700-R (AEI/FEDER, UE), and by the Principality of Asturias Government under project FC-15-GRUPIN14-073. P.E.D.S.R. and R.V. acknowledge the Spanish Ministry of Economy and Competitiveness (grants CTQ2014-58989-P and CTQ2015-71936-REDT).

REFERENCES

1. Miller, J. R.; Simon, P. *Science* **2008**, *321*, 651.
2. Simon, P.; Gogotsi, Y. *Nat. Mater.* **2008**, *7*, 845.
3. Liu, C.; Li, F.; Ma, L. P.; Cheng, H. M. *Adv. Mater.* **2010**, *22*, E28.
4. Kaempgen, M.; Chan, C. K.; Ma, J.; Cui, Y.; Gruner, G. *Nano Lett.* **2009**, *9*, 1872.
5. Winter, M.; Brodd, R. *J. Chem. Rev.* **2004**, *104*, 4245.
6. Shi, W.; Zhu, J.; Sim, D. H.; Tay, H. H.; Lu, Z.; Zhang, X.; Sharma, Y.; Srinivasan, M.; Zhang, H.; Hng, H. H.; Yan, Q. *J. Mater. Chem.* **2011**, *21*, 3422.
7. Hu, C. C.; Chang, K. H.; Lin, M. C.; Wu, Y. T. *Nano Lett.* **2006**, *6*, 2690.
8. Ke, Y. K.; Tsai, Y. S.; Huang, Y. S. *J. Mater. Chem.* **2005**, *15*, 2122.
9. Xiao, W.; Xia, H.; Fuh, J. Y. H.; Lu, L. *J. Power Sources* **2009**, *193*, 935.
10. Abouimrane, A.; Compton, O. C.; Amine, K.; Nguyen, S. T. *J. Phys. Chem. C* **2010**, *114*, 12800.
11. Yan, J.; Fan, Z. J.; Wei, T.; Qian, W. Z.; Zhang, M. L.; Wei, F. *Carbon* **2010**, *48*, 3825.
12. Xia, K. S.; Gao, Q. M.; Jiang, J. H.; Hu, J. *Carbon* **2008**, *46*, 1718.
13. Frackowiak, E. *Phys. Chem. Chem. Phys.* **2007**, *9*, 1774.
14. Frackowiak, E.; Metenier, K.; Bertagna, V.; Beguin, F. *Appl. Phys. Lett.* **2000**, *77*, 2421.
15. Du, C. S.; Pan, N. *Nanotechnology* **2006**, *17*, 5314.
16. Zhang, L. L.; Zhao, X. S. *Chem. Soc. Rev.* **2009**, *38*, 2520.
17. Zhu, J. X.; Sun, T.; Hng, H. H.; Ma, J.; Boey, F. Y. C.; Lou, X. W.; Zhang, H.; Xue, C.; Chen, H. Y.; Yan, Q. *Chem. Mater.* **2009**, *21*, 3848.
18. Wu, N. L. *Mater. Chem. Phys.* **2002**, *75*, 6.
19. Cottineau, T.; Toupin, M.; Delahaye, T.; Brousse, T.; Belanger, D. *Appl. Phys. A: Mater. Sci. Process.* **2006**, *82*, 599.
20. Jiang, J. H.; Kucernak, A. *Electrochim. Acta* **2002**, *47*, 2381.
21. Toupin, M.; Brousse, T.; Belanger, D. *Chem. Mater.* **2004**, *16*, 3184.

22. Roberts, A. J.; Slade, R. C. T. *J. Mater. Chem.* **2010**, *20*, 3221.
23. Hu, C.-C.; Chang, K.-H.; Lin, M.-C.; Wu, Y.-T. *Nano Lett.* **2006**, *6*, 2690.
24. Li, G.-R.; Feng, Z.-P.; Ou, Y.-N.; Wu, D.; Fu, R.; Tong, Y.-X. *Langmuir* **2010**, *26*, 2209.
25. Yuan, G. H.; Jiang, Z. H.; Aramata, A.; Gao, Y. Z. *Carbon* **2005**, *43*, 2913.
26. Gujar, T. P.; Shinde, V. R.; Lokhande, C. D.; Kim, W. Y.; Jung, K. D.; Joo, O. S. *Electrochem. Commun.* **2007**, *9*, 504.
27. Selvan, R. K.; Perelshtein, I.; Perkas, N.; Gedanken, A. *J. Phys. Chem. C* **2008**, *112*, 1825.
28. Wang, K.; Huang, J.; Wei, Z. *J. Phys. Chem. C* **2010**, *114*, 8062.
29. Ryu, K. S.; Kim, K. M.; Park, N. G.; Park, Y. J.; Chang, S. H. *J. Power Sources* **2002**, *103*, 305.
30. Mastragostino, M.; Arbizzani, C.; Soavi, F. *J. Power Sources* **2001**, *97–98*, 812.
31. Lehtimäki, S.; Suominen, M.; Damlin, P.; Tuukkanen, S.; Kvarnström, C.; Lupo, D. *ACS Appl. Mater. Interfaces* **2015**, *7* (40), 22137.
32. Park, S.; An, J.; Jung, I.; Piner, R. D.; An, S. J.; Li, X.; Velamakanni, A.; Ruoff, R. *Nano Lett.* **2009**, *9*, 1593.
33. Zeng, X.; Yang, J.; Yuan, W. *Eur. Polym. J.* **2012**, *48*, 1674.
34. Pham, V. H.; Dang, T. T.; Hur, S. H.; Kim, E. J.; Chung, J. S. *ACS Appl. Mater. Interfaces* **2012**, *4*, 2630.
35. Conway, B. E. *Electrochemical Supercapacitors: Scientific Fundamentals and Technological Applications*; Springer: New York, **1999**.
36. Wang, S. Y.; Ho, K. C.; Kuo, S. L.; Wu, N. L. *J. Electrochem. Soc.* **2006**, *153*, A75.
37. Wohlfahrt-Mehrens, M.; Schenk, J.; Wilde, P. M.; Abdelmula, E.; Axmann, P.; Garche, J. *J. Power Sources* **2002**, *105*, 182.
38. Wu, N. L. *Mater. Chem. Phys.* **2002**, *75*, 6.
39. Chang, J.; Lee, W.; Mane, R. S.; Cho, B. W.; Han, S. H. *Electrochem. Solid-State Lett.* **2008**, *11*, A9.
40. Shirshova, N.; Qian, H.; Shaffer, M. S. P.; Steinke, J. H. G.; Greenhalgh, E. S.; Curtis, P. T.; Kucernak, A.; Bismarck, A. *Composites, Part A* **2013**, *46*, 96.
41. Qian, H.; Diao, H.; Shirshova, N.; Greenhalgh, E. S.; Steinke, J. H. G.; Shaffer, M. S. P.; Bismarck, A. *J. Colloid Interface Sci.* **2013**, *395*, 241.
42. Shirshova, N.; Qian, H.; Houllé, M.; Steinke, J. H. G.; Kucernak, A. R. J.; Fontana, Q. P. V.; Greenhalgh, E. S.; Bismarck, A.; Shaffer, M. S. P. *Faraday Discuss.* **2014**, *44*, 81.
43. Senokos, E.; Reguero, V.; Palma, J.; Vilatela, J. J.; Marcilla, R. *Nanoscale* **2016**, *8*, 3620.
44. Si, Y.; Samulski, E. T. *Chem. Mater.* **2008**, *20*, 6792.
45. Qian, H.; Kucernak, A. R.; Greenhalgh, E. S.; Bismarck, A.; Shaffer, M. S. P. *ACS Appl. Mater. Interfaces* **2013**, *5*(13), 6113.
46. Liu, Q.; Nayfeh, M. H.; Yau, S. T. *J. Power Sources* **2010**, *195*, 7480.
47. Bohm, D. *Quantum Theory*; Dover: New York, **1989**.
48. Simmons, J. G. *J. Appl. Phys.* **1963**, *34*, 1793.
49. Zabihi, Z.; Araghi, H. *Synth. Metals* **2016**, *217*, 87.